

Stability of bedforms in laminar flows with free surface: from bars to ripples

O. DEVAUCHELLE^{1,2†}, L. MALVERTI¹,
É. LAJEUNESSE¹, P.-Y. LAGRÉE³,
C. JOSSERAND³ AND K.-D. NGUYEN THU-LAM³

¹Institut de Physique du Globe, 4 place Jussieu, 75252 Paris cedex 05, France

²Earth, Atmospheric and Planetary Science, Massachusetts Institute of Technology,
77 Massachusetts Avenue, Cambridge, MA 02139-4307, USA

³Institut Jean le Rond d'Alembert, CNRS, Université Pierre et Marie Curie, Boîte 161–162,
Tour 55–65, 4 Place Jussieu, 75252 Paris Cedex 05, France

(Received 5 December 2008; revised 25 August 2009; accepted 28 August 2009)

The present paper is devoted to the formation of sand patterns by laminar flows. It focuses on the rhomboid beach pattern, formed during the backwash. A recent bedload transport model, based on a moving-grains balance, is generalized in three dimensions for viscous flows. The water flow is modelled by the full incompressible Navier–Stokes equations with a free surface. A linear stability analysis then shows the simultaneous existence of two distinct instabilities, namely ripples and bars. The comparison of the bar instability characteristics with laboratory rhomboid patterns indicates that the latter could result from the nonlinear evolution of unstable bars. This result, together with the sensibility of the stability analysis with respect to the parameters of the transport law, suggests that the rhomboid pattern could help improving sediment transport models, so critical to geomorphologists.

Key words: absolute/convective, lubrication theory/thin films, sediment transport

1. Introduction

When water flows above a granular layer, the interaction between sediment transport and the fluid motion often leads to instability patterns such as ripples, dunes and bars (see Allen 1982). This is well known in rivers, where the flow is turbulent, but this is true as well at lower Reynolds number. The most widespread example of a sediment pattern generated by a laminar flow is the ubiquitous rhomboid beach pattern (see Woodford 1935; Devauchelle *et al.* 2009). One can observe the formation of these diamond-shaped structures after the swash, when water returns to the sea through a thin film covering the sand. The rhomboid pattern has been found also in geological records (Thompson 1949; Singh 1969), where it may be misinterpreted as the crossing of two successive sets of ripples (Williamson 1887).

Rhomboid beach patterns are generally associated with stationary gravity waves in supercritical inviscid flows. Woodford (1935) first suggested that the sand simply could be marked by such waves, thus neglecting the coupling between the sediment transport and the flow. This theory provides a relationship between the pattern angle α and the Froude number Fr , namely $\alpha = \arcsin(1/Fr)$. Most subsequent

† Email address for correspondence: devauche@mit.edu

contributions on the subject (Chang & Simons 1970; Allen 1982) are based on the same idea. However, Devauchelle *et al.* (2009) showed experimentally that Woodford's law strongly overpredicts the pattern angle. Ikeda (1983) proposed that the rhomboid pattern might result from the association of antidunes and longitudinal striations. This idea will be addressed in the present paper (see §3.3).

After their own experimental observations, Karcz & Kersey (1980) concluded that a homogeneous rhomboid pattern forms spontaneously over an initially flat bed, thus suggesting an absolute instability. In a first attempt to perform the stability analysis of a granular bed submitted to erosion by a laminar film, we have used the Saint-Venant approximation to model the water flow. This model was expected to generate a rhomboidal pattern under laminar conditions, as it does under turbulent ones (see Defina 2003; Hall 2006). And indeed the shallow-water theory for laminar flows does predict that a bar instability should develop. In turn, this instability leads to diamond-shaped structures after saturation, due to nonlinear effects. In that sense, the rhomboid beach pattern can be related to alternate bars in rivers (Callander 1969).

However, the Saint-Venant equations fail to predict the pattern angle better than the Woodford's law does. Contrary to the latter, the Saint-Venant model underpredicts the pattern angle by a factor of about 3. The results are even worse regarding the wavelength, but the theory at least qualitatively agrees with the observation of Karcz & Kersey (1980) that a uniform wavelength spontaneously emerges.

The main flaw of the classical Saint-Venant equations regarding bedforms is that they cannot represent the phase lag between a bed perturbation and the velocity profile above it. When establishing the Saint Venant equations, one supposes that this profile remains parabolic (Poiseuille flow). However, due to the acceleration over the crest of the ripple, the velocity profile changes near the bed. This effect is responsible for the formation of ripples (see Kennedy 1963; Charru & Mouilleron-Arnould 2002; Lagrée 2003), which appeared regularly during the experiments of Devauchelle *et al.* (2009) (see also figure 1). This observation suggests that the shallow-water approximation is inappropriate under such experimental conditions, at least in its simplest form. In the present contribution, we replace this approximation by the full Navier–Stokes equations in three dimensions.

An alternative method would consist in replacing the standard shallow-water equations by the more elaborate but still two-dimensional model of Scheid, Ruyer-Quil & Manneville (2006), which keeps track of the vertical flow motion. However, for the linear stability analysis presented here, the full Navier–Stokes equations are of much simpler use.

Coupling the water flow to the bed evolution requires a sediment transport model. As long as bedload is the main transport mode, the grains motion is driven by the water shear stress on the sediment surface only. Transport laws are generally written as functions of the Shields parameter, which compares the tangential shear applied to the bed to its normal counterparts (usually the weight of the upper grains layer, see Shields 1936). However, in order to avoid the instability of short-wavelength bedforms, one has to introduce a stabilizing mechanism. This can be achieved by taking into account either the bed slope effect or the distance required for the particles flux to reach equilibrium (Lagrée 2000; Charru, Mouilleron & Eiff 2004; Charru 2006; Charru & Hinch 2006). The present paper generalizes the model proposed by Charru (2006) to three dimensions, thus retaining both saturation mechanisms. As the full Navier–Stokes equations are employed, no strong approximation about the flow remains. For this reason, the rhomboid pattern can provide an experimental test for sediment transport models.

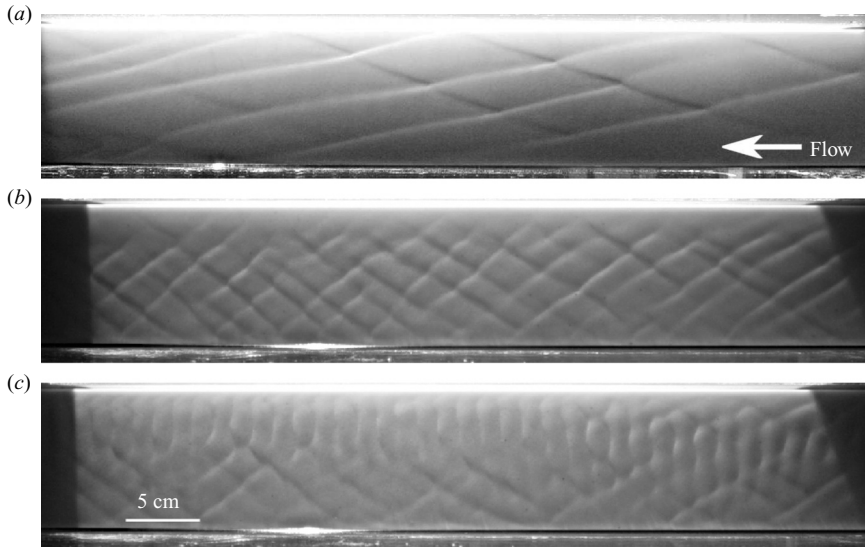


FIGURE 1. Various bedforms observed on the granular bed of a laminar flume (Devauchelle *et al.* 2009). The flow is from right to left. The pattern, observed through the water surface, is enhanced by skimming light. The angle and wavelength of the rhomboid pattern varies with the experimental parameters ((a) and (b)). Under certain conditions, ripples can coexist with a rhomboid pattern (c). The width of the flume is 10 cm. (a) Large rhomboid pattern ($Fr = 1.76$, $S = 0.03$, $Bo = 1.31$ and $Sh = 0.616$). (b) Small rhomboid pattern ($Fr = 0.95$, $S = 0.015$, $Bo = 3.25$ and $Sh = 0.485$). (c) Rhomboid pattern mixed with ripples ($Fr = 1.01$, $S = 0.015$, $Bo = 3.50$ and $Sh = 0.504$). The definitions of the parameters are provided in § 3.2.

2. General model

We aim here to study the linear stability of an initially flat sediment layer, as a laminar and steady film of water flows over it. Our primary objective is to derive a model of the experiments presented in Devauchelle *et al.* (2009). Nevertheless, since the rhomboidal pattern observed in the laboratory is extremely similar to natural rhomboid patterns, chances are that the present model would also describe some of them. Besides the laminar flow assumption, we also require that the flow is not influenced by the roughness of the granular bed. In other words, the typical grain size must remain negligible with respect to the water film thickness. This was true during the experiment, performed with a $75\ \mu\text{m}$ sand. Stauffer, Hajnal & Gendzwil (1976) report natural rhomboidal patterns on beaches where the typical grain size ranges from $100\ \mu\text{m}$ to more than 1 mm. The applicability of the present model to natural patterns depends on the flow depth, which is not easily measured on the field.

For simplicity, we assume an infinite system both in the direction x of the main slope and in the transverse direction y (see figure 2). This is consistent with the usual configuration of sand beaches where rhomboid patterns form, where the horizontal dimensions (say a few metres) are far larger than the typical depth D of the backwash film (a few millimetres). It may however be a crude representation of the experiments of Devauchelle *et al.* (2009), performed in a 10 cm wide channel.

2.1. Water flow

The main flow direction is denoted x , and its transverse and vertical counterparts are y and z respectively. The sediment surface is represented by $h(x, y, t)$, and the fluid free surface by $\eta(x, y, t)$. The whole frame is tilted with respect to gravity in

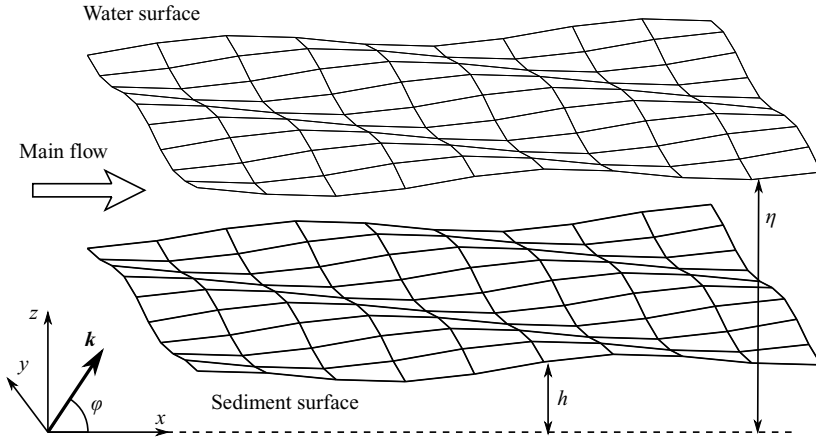


FIGURE 2. Schematic of the system and associated notations. A film of fluid with a free surface flows over a granular layer. In § 3, the stability of a perturbation with wave vector \mathbf{k} is analysed.

the x direction, so that the gravity acceleration \mathbf{g} has components $(g_x, g_z, 0)$ with $-g_x/g_z = \tan S$, thus defining the slope S .

The flow in the bulk is given by the stationary and incompressible Navier–Stokes equations in three dimensions,

$$u_k \partial_k u_i = -\frac{1}{\rho} \partial_i p + g_i + \nu \partial_{kk} u_i, \quad \partial_k u_k = 0, \quad (2.1)$$

where \mathbf{u} , p and ν are respectively the velocity, pressure and viscosity of water, and \mathbf{g} is the acceleration of gravity. The use of stationary flow equations is a common hypothesis in geomorphology, which requires that the bedform-evolution time scale be much larger than the flow one (see Colombini & Stocchino 2005). As a consequence of this hypothesis, the characteristic time scale (which will be defined in § 3) is based only on the sediment transport.

If we neglect both the velocity of the upper layers of grains and the velocity of water through the same layer, we may impose the classical no-slip boundary condition at the sediment bed surface. This assumption is reasonable in the experiments. It has been evaluated by comparing the measured flow depth to Nußelt's prediction for a given water discharge. Then,

$$u_i = 0 \quad \text{at} \quad z = h, \quad (2.2)$$

where z is the direction perpendicular to the (x, y) plane, which is slightly tilted in the x direction (hereafter named *vertical*), and h is the thickness of the sediment layer. At the free surface, which elevation is denoted by η , both a kinematic and a dynamical boundary conditions are imposed:

$$u_z = u_x \partial_x \eta + u_y \partial_y \eta \quad \text{at} \quad z = \eta, \quad \sigma_{ik} n_k = \gamma \kappa n_i \quad \text{at} \quad z = \eta, \quad (2.3)$$

where γ and \mathbf{n} are respectively the surface tension of the fluid, and the unit vector normal to the surface and pointing outwards. The free-surface curvature is referred to as κ , which is linked to the surface elevation through the relation

$$\kappa = \frac{\partial_{xx} \eta}{(1 + (\partial_x \eta)^2)^{3/2}} + \frac{\partial_{yy} \eta}{(1 + (\partial_y \eta)^2)^{3/2}}. \quad (2.4)$$

The stress tensor is denoted by σ , whereas τ is its viscous component only:

$$\sigma_{ik} = \tau_{ik} - p\delta_{ik}, \quad \tau_{ik} = \rho\nu(\partial_i u_k + \partial_k u_i). \quad (2.5)$$

The flow model presented above is rather general for gravity-driven and laminar films. The stability of such films, without any sediment transport, has been intensively studied, and they were proven generally unstable with respect to long-wavelength perturbations (Yih 1963), leading to the formation of Kapitza waves (Kapitza 1948). Such films present a wide variety of unstable waves, stationary or not. Indeed, Kapitza waves are linearly unstable in two dimensions, but one can expect three-dimensional structures to be also linearly unstable (Lin & Chen 1997). One could claim that such purely hydrodynamic waves generate the rhomboid pattern, in what would be an extended version of the theory of Woodford (1935). However, the present flow model is stationary, and thus cannot describe any purely fluid instability. Only in the next section on sediment transport will time enter the picture. Consequently, the stability analysis of the present paper can only account for a fully coupled sediment-flow interaction. During their experiments, Devauchelle *et al.* (2009) observed both stationary and travelling hydraulic waves. None of them seemed to interact much with the sediment patterns, which grew at a much slower time scale and with a different angle than these waves.

2.2. Sediment transport

Various sediment transport models based on a grains balance in the moving sediment layer have been proposed, both for liquid flows (Lagrée 2000) and for air flows (Valance & Rioual 1999; Sauermann, Kroy & Herrmann 2001; Andreotti, Claudin & Douady 2002; Hersen 2004), and widely developed for viscous flows by Charru *et al.* (2004). The latter authors were able to measure the individual grains velocities during bedload transport. Their model for averaged transport is thus supported experimentally at each step of its derivation. The last version of this theory has been adapted to gently sloping beds (Charru 2006; Charru & Hinch 2006). Values are provided for the empirical coefficients of the theory, that allow to fit the experimental data of Coleman & Eling (2000). In the present section, we aim to generalize this model in three dimensions, by following the reasoning of Charru (2006). We will end up with the remarkable result that no additional coefficient is required to do so.

Let us denote by n the density of transported particles per unit surface. Then the grains balances in the bedload layer and for the motionless grains read

$$\frac{\partial n}{\partial t} = \dot{n}_e - \dot{n}_d - \frac{\partial q_x}{\partial x} - \frac{\partial q_y}{\partial y}, \quad C\partial_t h = -\frac{\pi d_s^3}{6}(\dot{n}_e - \dot{n}_d), \quad (2.6)$$

where \dot{n}_e , \dot{n}_d and \mathbf{q} denote respectively the rate of grains erosion from the fixed layer, the deposition rate to the fixed layer and the horizontal grains flux. The bed compactness is denoted by C . At first order, and for small bed slopes, this equation does not differ from the flat-bed case, even though the direction of \mathbf{q} no longer belongs to the (x, y) plane. For bedload on an arbitrary sediment surface, the flux \mathbf{q} is tangent to the surface. Its horizontal components q_x and q_y only must be considered in the Exner equation.

If we assume that the moving layer is dilute enough for the grain-grain interaction to be negligible, then the deposition rate is proportional to the number of suspended

particles times the Stokes settling velocity U_s :

$$\dot{n}_d = c_d \frac{U_s}{d_s} n, \quad U_s = \frac{(\rho_s - \rho) \|\mathbf{g}\| d_s^2}{18\rho\nu}, \quad (2.7)$$

where c_d is an empirical constant, set to 1/15 after Charru (2006).

Originally, the Shields parameter was designed to compare the weight of a sediment particle (corrected by its buoyancy) to the shear stress exerted by the fluid (Shields 1936), that is

$$Sh = \frac{\rho \|\boldsymbol{\tau}_h\|}{(\rho_s - \rho) \|\mathbf{g}\| d_s}, \quad (2.8)$$

where d_s is the typical diameter of a sediment grain, and ρ_s is the density of the sediment. The tensor $\boldsymbol{\tau}_h$ represents the horizontal viscous stress. Now, if the local tilt of the sediment bed is to be considered, one has to compare the normal stress component to the tangential one instead. It is the purpose of the following.

If \mathbf{n}^b is the unit vector normal to the sediment surface, then the viscous force exerted on a surface of small area ϵ of the sediment surface reads

$$f_i^v = \tau_{ik} n_k^b \epsilon. \quad (2.9)$$

If the pressure field is uniform at the grain scale, gravity is the only other force acting on the moving grains layer, the thickness of which is denoted by $c_g d_s$:

$$f_i^g = (\rho_s - \rho) g_i \epsilon c_g d_s. \quad (2.10)$$

The total force $\mathbf{f} = \mathbf{f}^v + \mathbf{f}^g$ may then be separated into its normal and tangential components:

$$f^n = f_k n_k^b, \quad \mathbf{f}^t = \mathbf{f} - f^n \mathbf{n}^b. \quad (2.11)$$

Note that f^n is a negative quantity. In this frame, the natural generalization of Shields parameter consists in writing

$$\theta = -\frac{\|\mathbf{f}^t\|}{f^n}. \quad (2.12)$$

Through this definition of the Shields parameter, one recovers the two-dimensional theory of Charru (2006) when considering a two-dimensional problem in the (x, z) plane. In that sense, the present model is a generalization of the latter. The hypothesis that θ only controls the intensity of the sediment flux relies on two basic assumptions:

- (i) the effect of slope is isotropic with respect to x and y ;
- (ii) the thickness $c_g d_s$ of the moving grains layer is constant.

The first assumption is reasonable in general, whereas we are not aware of any direct evaluation of the moving-grains layer thickness. Charru (2006) makes the second assumption when stating that c_g is a constant. As long as the bed is perfectly flat, the moving-grains layer thickness itself can be a function of the Shields parameter as usually defined (i.e. by (2.8)), and thus the intensity of the transport is a function of Sh only. As soon as some slope is considered, it enters the picture as a new independent parameter, and the above reasoning should not hold. However, Charru (2006) showed that treating c_g as a constant can lead to good results. We do the same here.

We usually consider that the erosion rate \dot{n}_e vanishes below a threshold value of the Shields parameter, denoted by θ_t . Above this value, the simplest model consists in assuming that the number of particles suspended by unit time and surface is proportional to the excess Shields parameter $Sh - \theta_t$. If we apply this idea to the generalized Shields parameter, we thus assume that \dot{n}_e is proportional to $c_g \theta - \theta_t$. The

constant c_g appears only due to our definition of θ . Indeed, c_g sets the thickness of the moving layer, and thus has an impact on the normal to tangential forces ratio. As it varies and it is hard to measure, this quantity has been removed traditionally from the definition of the Shields parameter, and embedded in the transport law. We cannot use such a simplification here. With these notations, the threshold value remains the one proposed by Charru (2006), namely $\theta_t \approx 0.091$. The choice of the dimensional prefactors then fixes the empirical constant c_e :

$$\dot{n}_e = \frac{18c_e U_s}{d_s^3} (c_g \theta - \theta_t). \quad (2.13)$$

Charru (2006) fixes c_e to 0.0017, but we will see that this value has no impact on the pattern shape in the linear theory. In the above relation, the slope influence on the tangential shear stress is embedded into the definition of θ .

While they are detached from the bed, the grains are transported by the water flow, thus generating a horizontal sediment flux \mathbf{q} . The order of magnitude of the flow velocity near the bed scales with the diameter of the grains and the shear $d_s \partial_z u_x$. The flux is then proportional to the concentration of moving particles n times this typical velocity:

$$q_x = n c_u d_s \frac{\partial u_x}{\partial z}, \quad q_y = n c_u d_s \frac{\partial u_y}{\partial z}, \quad (2.14)$$

where $c_u \approx 0.1$ is the fifth and last empirical parameter of the sediment transport law. This hypothesis can be understood as a simplified version of Bagnold's model of sediment transport by rivers (Bagnold 1977).

In order to remain consistent with the stationary flow model (see §2.1), we must drop the time derivative in the sediment balance equation (2.6). Thus, the particle flow is considered stationary as well and we end up with the well-known Exner equation (Exner 1925):

$$C \partial_t h = -\frac{\pi d_s^3}{6} (\partial_x q_x + \partial_y q_y). \quad (2.15)$$

One should bear in mind that the above equation, a balance for the immobile grains, does not replace the balance (2.6) for mobile grains. The latter is required to determine the moving particle density n , even under the quasi-stationary approximation. In brief, one can determine the concentration of moving particles using (2.6) with the quasi-stationary approximation $\partial n / \partial t = 0$. Then, (2.15) controls the topography evolution.

The Exner equation terminates the definition of our sediment transport model, and the following section is devoted to the stability analysis of a flat bed within this framework.

3. Stability analysis

The present section aims to demonstrate that, under the experimental conditions where rhomboid patterns were observed by Devauchelle *et al.* (2009), the model proposed above is unstable. As stated in the introduction of this paper, it is our claim that the rhomboid pattern can maintain its basic features (angle and wavelength) during its development. In other words, we believe (but do not prove) that the nonlinear effects allowing for the bed perturbations to saturate do not modify significantly these features. If this is true, the results of the stability analysis can be compared to measurements (see §4), even though the latter concerns fully developed bedforms rather than infinitesimal perturbations.

3.1. Base state and dimensions

The simplest base state for our system consists in a flat (but tilted) sediment bed, over which flows a uniform Nußelt film of thickness D . This roughly corresponds both to the experiments (a rake was drawn over the granular bed before each run), and to the natural initial condition on beaches (each swash event erases the remaining patterns before the backwash). Assuming the grain size is small enough to do so, we neglect the bed roughness here.

The Nußelt film above the bed reads

$$u_x^0 = \frac{g_x}{\nu} \left(zD - \frac{z^2}{2} \right), \quad p^0 = -\rho g_z (D - z), \quad (3.1)$$

where the subscript 0 refers to the base state. The water velocity vanishes in both the y and the z directions. If \mathcal{U} , \mathcal{D} and \mathcal{P} respectively refer to the typical scales of the water velocity, depth and pressure, we define

$$\mathcal{U} = \frac{g_x}{3\nu} D^2, \quad \mathcal{D} = D, \quad \mathcal{P} = -\rho g_z D. \quad (3.2)$$

The non-dimensional base state then reads

$$u_x^0 = \mathcal{U} U \left(\frac{z}{D} \right), \quad p^0 = \mathcal{P} P \left(\frac{z}{D} \right) \quad (3.3)$$

with

$$U(\tilde{z}) = \frac{3\tilde{z}}{2} (2 - \tilde{z}), \quad P(\tilde{z}) = (1 - \tilde{z}). \quad (3.4)$$

The tilde here denotes a non-dimensional height. In the following, all quantities are non-dimensional, and the tilde will be dropped for clarity.

3.2. Perturbations

Let f refers to any quantity of interest for our problem (\mathbf{u} , p , h , η and \mathbf{q}). Decomposing it into a base-state component F and a sine-wave perturbation of complex amplitude $f^*(z)$ leads to

$$f(x, y, z, t) = F(z) + f^*(z) e^{i(k \cos \varphi x + k \sin \varphi y - \omega t)}, \quad (3.5)$$

where k , φ and ω are respectively the wave-vector norm, its angle with respect to the x axis, and the frequency of the perturbation. The non-dimensional wave vector is normalized by \mathcal{D} . In the same fashion, the time scale \mathcal{T} for the frequency ω is given by the Exner equation (2.15):

$$\mathcal{T} = \frac{6C\mathcal{D}^2}{\pi l_d c_d U_s d_s^2 N}, \quad (3.6)$$

where l_d and N are respectively the *deposition length* defined by Charru (2006), and the suspended concentration of the base flow:

$$l_d = \frac{3c_u \mathcal{U} d^2}{c_d U_s \mathcal{D}}, \quad N = \frac{18c_e}{c_d d_s^2} (c_g \Theta - \theta_t). \quad (3.7)$$

The deposition length, which corresponds to the order of magnitude of the average flight length of a particle, introduces a space gap between the sediment flux and the shear stress that generates it. This delay stabilizes the perturbations at short wavelengths (Andreotti *et al.* 2002; Charru & Mouilleron-Arnould 2002; Lagrée 2003). Its relationship with the saturation length used in dune models is discussed

by Charru (2006). With these notations, one recovers the steady state sediment flux (saturated flux)

$$q_s = c_u d_s N \partial_z u_x. \quad (3.8)$$

3.2.1. Linearized flow equations

For small perturbations, the momentum- and mass-conservation equations for the fluid (2.1) read

$$Fr^2(iUk \cos \varphi u_x + U' u_z) = -ik \cos \varphi p + \frac{S}{3}(u_x'' - k^2 u_x), \quad (3.9)$$

$$Fr^2 iUk \cos \varphi u_y = -ik \sin \varphi p + \frac{S}{3}(u_y'' - k^2 u_y), \quad (3.10)$$

$$Fr^2 iUk \cos \varphi u_z = -p' + \frac{S}{3}(u_z'' - k^2 u_z), \quad (3.11)$$

$$u_z' + ik(\cos \varphi u_x + \sin \varphi u_y) = 0, \quad (3.12)$$

where $Fr = \mathcal{U}/\sqrt{-g_z \mathcal{D}}$ is the Froude number. The prime denotes derivation with respect to the non-dimensional height z . The no-slip boundary condition (2.2) at the bed surface in turn reads

$$u_x + 3h = 0, \quad u_y = 0, \quad u_z = 0. \quad (3.13)$$

At the free surface, the kinematic boundary condition imposes

$$u_z = \frac{3}{2} ik \cos \varphi \eta, \quad (3.14)$$

whereas the dynamic boundary condition reads

$$-3\eta + u_x' + ik \cos \varphi u_z = 0, \quad ik \sin \varphi u_z + u_y' = 0, \quad \eta - p + \frac{2}{3} S u_z' = -\frac{k^2}{Bo} \eta, \quad (3.15)$$

where $Bo = -g_z \rho \mathcal{D}^2 / \gamma$ is the Bond number.

3.2.2. Linearized sediment transport equations

Combining the definition of the concentration scale N with the linearized grains balance relation for stationary sediment transport (2.6) leads to

$$\frac{\Theta}{\Theta - \theta_i / c_g} \theta^* - n^* - \frac{c_u \mathcal{U}}{c_d U_s} \left(\frac{d_s}{\mathcal{D}} \right)^2 ik(\cos \varphi (3n^* + u_x^{*'}) + \sin \varphi u_y^{*'}) = 0, \quad (3.16)$$

where the generalized Shields parameter for the base state Θ reads

$$\Theta = \frac{Sh}{c_g} + S = \frac{3\mathcal{U}v\rho}{c_g d |g_z| \mathcal{D} (\rho_s - \rho)} + S. \quad (3.17)$$

The perturbation θ^* for the Shields parameter is given by (2.12):

$$\theta^* = \frac{1}{3} \left(2 \left(\frac{Sh}{c_g} \right)^2 (u_z^{*'} - 3ih^* k \cos \varphi) - 3ih^* k \cos \varphi (1 + S^2) + \frac{Sh}{c_g} (u_x^{*'} + 2S u_z^{*'} - 3h^* (1 + 3ik \cos \varphi S)) \right). \quad (3.18)$$

Finally, the Exner equation (2.15) allows to close the linear system, as did (2.15) for the complete model:

$$\omega h^* = k(\cos \varphi (3n^* + u_x^{*'}) + \sin \varphi u_y^{*'}). \quad (3.19)$$

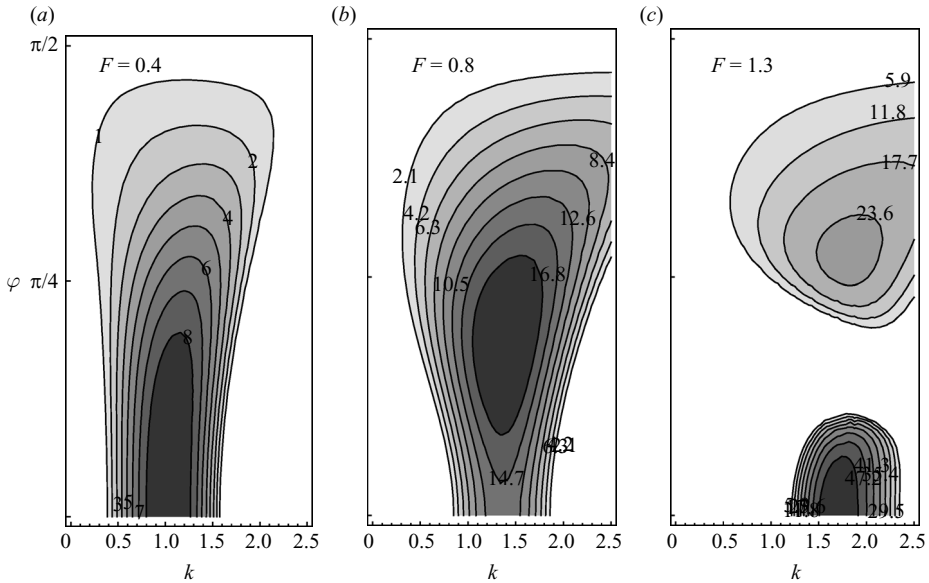


FIGURE 3. Growth rate $\text{Im}(\omega)$ of the three-dimensional instabilities of a granular bed submitted to erosion by a laminar flow, as a function of the wave-vector norm k , and angle φ with respect to the x direction. The blank domain corresponds to negative values of the growth rate, that is, stable modes. As the parameters vary (here only the Froude number does), the bar instability (a) and the ripple instability (b) alternatively dominate the system; and their coexistence is exhibited (c). In this example, the flow parameters have values $S=0.02$, $Bo=1$, $Sh=0.5$ and $\mathcal{U}d_s^2/(U_s\mathcal{D}^2)=0.05$. The transport law parameters are set to $\theta_t=0.091$, $c_u/c_d=1.5$ and $c_g=0.11$.

In this linear theory, only three out of five coefficients need to be fixed in order to define the sediment transport law (θ_t , c_u/c_d and c_g). The two remaining parameters are embedded into the definition of the characteristic time \mathcal{T} .

3.3. General features of the bed stability

The system of ordinary differential equations (3.10)–(3.12) is linear. For any wave vector \mathbf{k} , it can thus be solved numerically by means of the linear shooting method to fit the boundary conditions (3.13)–(3.15). Likewise, once the sediment transport law is defined by its empirical parameters θ_t , c_u/c_d and c_g (respectively 0.091, 0.9 and 0.108 in the present case), one can derive the complex frequency ω from (3.16), (3.18) and (3.19). Finally, for a given set of experimental parameters S , Fr , Bo and Sh , the dispersion relation of our system is obtained.

3.3.1. Ripples and bars

The dispersion relation for the bed perturbation provides informations about both the velocity of sand waves and their stability. In the present paper, we will focus on stability issues, since the associated predictions (pattern angle and wavelength) are easily measured experimentally.

The growth rates of three typical examples are plotted on figure 3. In the range of parameters that we have explored, the system is typically unstable. The relation dispersion always presents at least one positive maximum, and sometimes two. The position, existence and relative importance of these maxima depend strongly on all the flow parameters, and in a non-trivial way. The simultaneous existence of two

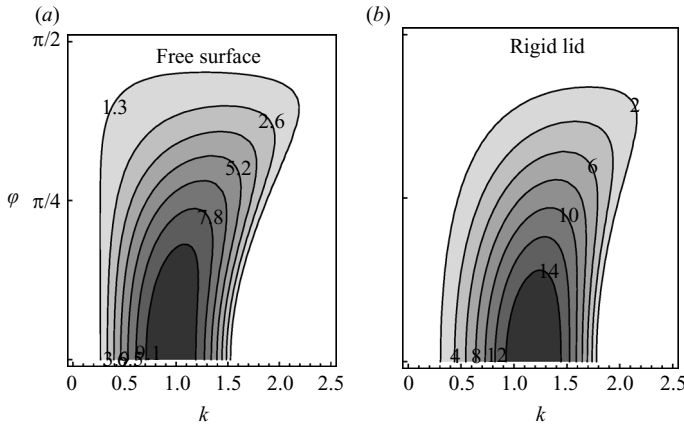


FIGURE 4. Influence of the free surface on the ripple instability ($Re = 27$ and $S = 0.01$ for both plots). (a) The flow has a free surface, with vanishing surface tension ($Bo \rightarrow \infty$). (b) The flow is covered with a rigid lid, at $\tilde{z} = 2$, so that the base-flow profile is the complete Poiseuille parabola, which lower half corresponds exactly to the Nusselt film of the free-surface case. The values of the other flow parameters are the same as in figure 3.

distinct instabilities allows us to propose the following definitions, which we think are consistent with the common use in the literature:

- (i) ripples correspond to a growth rate maximum lying on the k -axis, that is, for $\varphi = 0$;
- (ii) bars correspond to any other maximum.

The formation of sand ripples has received much attention, as an ubiquitous geomorphological pattern, since the early works of Exner (1925), Kennedy (1963) and Reynolds (1965). The mechanism leading to the ripple instability is now clearly established. It is similar in laminar (see Charru & Mouilleron-Arnould 2002; Lagrée 2003) and turbulent flows (see Colombini 2004; Elbelrhiti, Claudin & Andreotti 2005). Its basics can be reduced to the (x, z) plane, that is, in the main flow and vertical directions. On the windward side of a bump, the water inertia draws the flow lines closer together, and the velocity increases. The reverse occurs on the leeward side. The shear stress being a combined effect of the velocity variation by the streamlines thinning, the net effect of the flow lines squeezing is to increase the skin friction on the windward side. Now, viscosity induces a slight asymmetry of the flow, which makes the skin friction extremal just before the crest (Lagrée 2003). The Exner equation (2.15) then indicates that deposition occurs just after the bump, thus growing the perturbation and moving it forwards. This process being two-dimensional, it can only create invariant structures in the transverse direction. The term *ripples* generally implies this y invariance, at least during the initiation stage. A second characteristic of the ripple-formation mechanism is that the velocity profile is locally strongly accelerated near the bed and then differs from the Poiseuille flow. This cannot be represented by the classical Saint-Venant equations (although some more subtle two-dimensional models can (Kouakou & Lagrée 2005; Scheid *et al.* 2006). It explains why any bed-stability analysis performed with the shallow-water equations predicts stable ripples at any wavelength (Devauchelle *et al.* 2009). Finally, ripples can grow in deep water or in a pipe, that is, without any free surface (see figure 4 and Kuru, Leighton & McCready 1995).

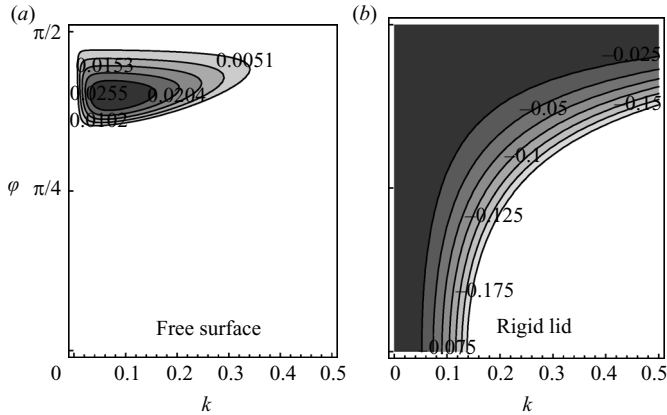


FIGURE 5. Influence of the free surface on the bar instability in a purely viscous flow ($Re = 0$ and $S = 0.02$ for both plots). (a) The flow has a free surface, with vanishing surface tension ($Bo \rightarrow \infty$). (b) The flow is covered with a rigid lid. In figure (b) the colour scale has been modified in order to show negative contours. The values of the other flow parameters are the same as in figure 3.

The three criteria listed above allow one to distinguish theoretically between ripples and pure bars. Contrary to ripples, bars can be modelled by means of the shallow-water approximation at first order (Devauchelle *et al.* 2007). Their wave vector is inclined with respect to the main flow direction (see figure 3), and thus cannot be represented in the (x, z) plane only. As shown on figure 5, bars can exist in purely viscous flows, for a vanishing Reynolds number. However, such viscous bars require a free surface, and would not appear in a pipe flow. When inertia plays a role, however, the picture is more complex: the bar instability can exist even when a rigid lid covers the flow. This instability disappears at low Reynolds number. We are not aware of any experimental observation of some bar-type pattern in a pipe flow.

Hereafter, the expression *pure bars* refers to the conceptual instability that can develop in purely viscous flows with free surface. In this sense, bars result from a combination of mechanisms involved in pure bar formation and mechanisms associated to ripples. To our knowledge, the first mathematical derivation of the bar instability is due to Callander (1969), and was soon associated to river meandering, although this point remains controversial (Ikeda, Parker & Sawai 1981; Blondeaux & Seminara 1985). Alternate bars in rivers are its most striking occurrence in Nature (Knaapen & Hulscher 2003). They result from the crossing of two bars instabilities of angle φ and $-\varphi$. It has been demonstrated, both experimentally (Lajeunesse *et al.* 2009) and theoretically (Devauchelle *et al.* 2007), that laminar flumes are also prone to similar bars development. Langlois & Valance (2005) performed a linear stability analysis comparable to the present one. However, their analysis was designed for a pipe flow, and thus did not include a free surface. As a consequence, their results are very similar to ours as far as the ripple instability is concerned, but did not show any bar instability.

Pure bars and ripples may be distinguished as two limiting cases of sediment-flows instability. However, in the range of parameters explored by Devauchelle *et al.* (2009) when studying rhomboid patterns, the two are mixed in a bar-type instability which presents some ripples features. Figure 6 illustrates this point. The first-order velocity field above a wavy bed corresponding to the bar instability is far from a parabola,

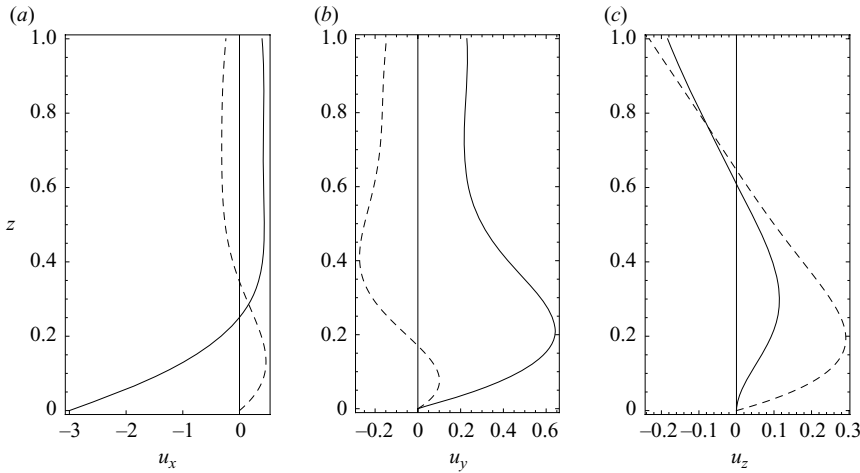


FIGURE 6. Complex velocities field for the bar instability. The solid line represents the real part of the velocity perturbation, whereas the dashed line represents its imaginary part. The shape of the perturbation in the full three-dimensional case differs significantly from the Nußelt parabola. These velocity profiles correspond to the maximum for the bar instability of figure 3 for $F = 0.8$, that is, $k = 1.38$ and $\varphi = 0.53$.

and thus could not be approached by means of the classical shallow-water equation, due to the strong influence of inertia. Within the nomenclature of the present paper, such bars are not pure bars.

3.3.2. Transition from bars to ripples

Figure 3 shows the evolution of bar and ripple instabilities with respect to the Froude number. Initially ($Fr = 0.4$ on figure 3), the only unstable mode corresponds to ripples. Now, if the Froude number is increased to $Fr = 0.8$, the growth-rate maximum leaves the $\varphi = 0$ axis, and consequently becomes a bar instability. Note that the dispersion relation being symmetrical with respect to the $\varphi = 0$ axis, this process splits the ripple instability into two symmetrical bar instabilities. If the Froude number is further increased, a ripple mode becomes unstable again, this time in association with the pre-existing bar instability. Rapidly, the maximum corresponding to ripples dominates.

Figure 7 shows the influence of the Froude number on the instabilities in more details. The splitting of the ripple instability described above is clearly apparent for a slope value of $S = 0.02$. However, this type of transition disappears if the slope is increased to $S = 0.03$. This behaviour illustrates the complexity of the parameters influence on the dispersion relation, thus explaining why Devauchelle *et al.* (2009) could not extract from the experiment a simple criterion for the transition from rhomboid patterns to ripples.

The theory proposed by Ikeda (1983) to describe the formation of rhomboid patterns in turbulent flumes must probably be rejected, at least in the laminar case. Instead of the interaction of ripples with longitudinal striations, we suggest that such pattern result from an instability which is a mixture of pure bars and ripples.

3.3.3. Sensitivity to the sediment transport law

The sediment transport law proposed by Charru (2006) involves five empirical parameters, namely θ_l , c_u , c_d , c_e and c_g . Its extension to three dimensions, exposed

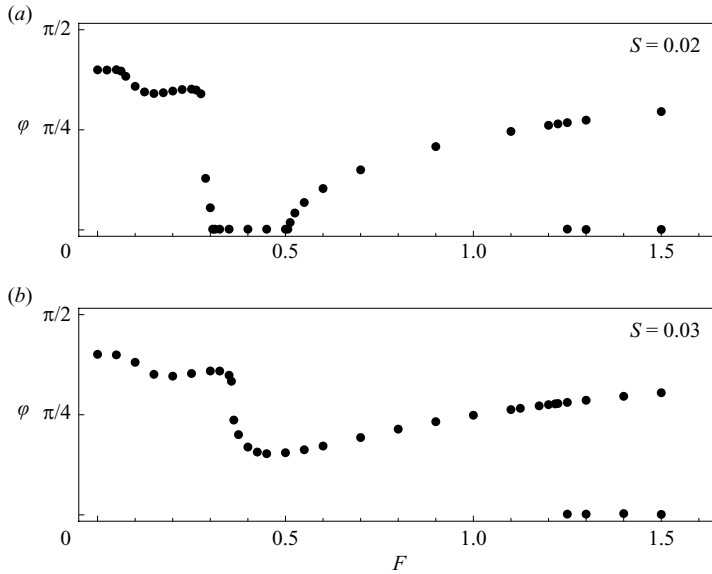


FIGURE 7. Angle φ of the local maxima of the dispersion relation as a function of the Froude number. The parameters other than the Froude number and the slope are those of figure 3.

in §2.2, does not increase their number. Both θ_t and $c_u c_e / c_d$ appear in the transport rate of stationary and uniform flows. They can thus be measured rather easily in experiments (Charru *et al.* 2004). Access to the others requires either direct measurement of the particles flux (Charru *et al.* 2004), or the study of some bed instability, as in the present work.

The geometrical properties of the unstable modes are fully determined by the parameters θ_t , c_u / c_d and c_g (see (3.16)–(3.19)). Figure 8 shows the theoretical variation of the pattern angle as a function of each of them. The ratio c_u / c_d has a decisive influence on the angle of the bar instability, even within the range of values proposed by (Charru *et al.* 2004), namely $[0.9, 2]$. This result was expected, since the deposition length l_d is proportional to c_u / c_d (see relation (3.7)). This characteristic length is believed to control the wavelength of ripples and dunes (Lagrée 2003; Elbelrhiti *et al.* 2005).

The influence of c_g is far more moderate, since it must be varied by orders of magnitude before influencing sensibly the instability pattern. Finally, the influence of the threshold Shields parameter θ_t is even weaker, and can safely be neglected in the entire possible range of this parameter (i.e. from $\theta_t = 0$ to the measured value of the Shields parameter, above which the theory becomes irrelevant).

Hereafter, both θ_t and c_g are set to the values proposed by Charru (2006) for low particle Reynolds numbers, namely $\theta_t = 0.09$ and $c_g = 0.11$. The ratio c_u / c_d is set to 1.5, an intermediate value between 0.9 and 2, which leads to better predictions than any of the two extreme values.

4. Comparison with flume-experiments data

The experimental apparatus used to reproduce the formation of rhomboid erosion patterns is presented in details in Devauchelle *et al.* (2009). The following section aims

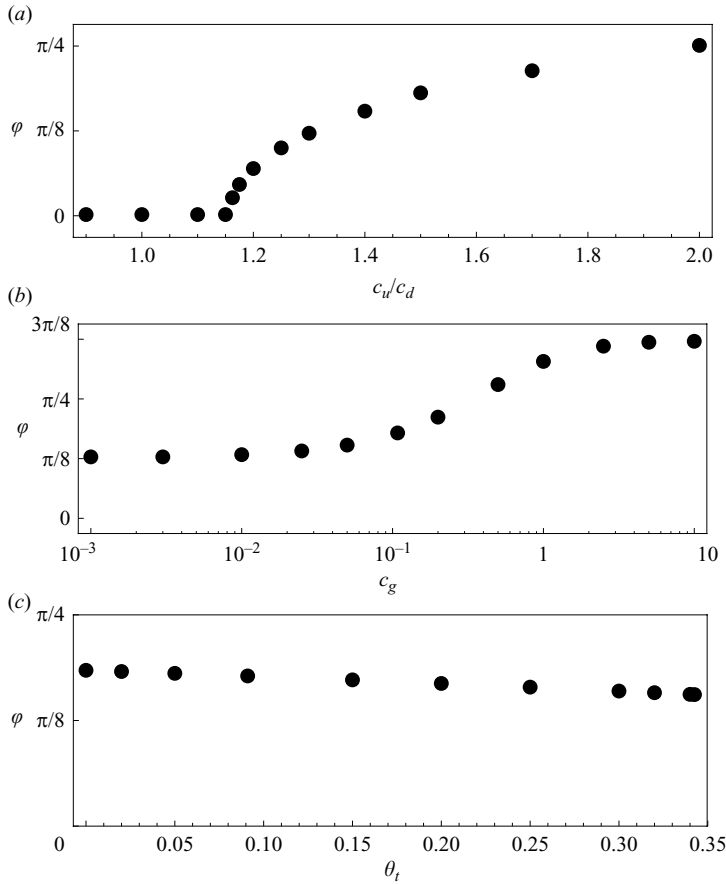


FIGURE 8. Sensibility of the bar instability mode with respect to the parameters of the sediment transport law. The black disks indicate the angle φ of the maximum. The flow parameters correspond to a real case, for which $F = 0.51$, $S = 0.02$, $Bo = 0.5$, $Sh = 0.34$ and $\mathcal{R}d_s^2/(U_s \mathcal{D}^2) = 0.08$. The transport law parameters are set to $\theta_t = 0.091$, $c_u/c_d = 1.5$ and $c_g = 0.11$, except naturally for the one involved in each plot.

only at a brief and general description, followed by comparison with the theoretical results presented above.

4.1. The experimental set-up

The experiments of Devauchelle *et al.* (2009) were performed in a small channel of length 240 cm and width 9.6 cm. The granular bed is made of silica beads of mean diameter 75 μm . The slope S in the flow direction x can be freely varied, as well as the water outflow. The flow depth never exceeds a few millimetres. The special features of this experiment are its small size, as well as the use of a mixture of glucose and water (the mixture viscosity ν varies between $10^{-6} \text{ m}^2 \text{ s}^{-1}$ and $5.6 \times 10^{-6} \text{ m}^2 \text{ s}^{-1}$). These two characteristics yields flows at low Reynolds number (generally a few tens, and always less than 500).

The surface tension γ of the water–glucose mixture was not measured during the experiments (the mass ratio of glucose to water was varied up to 50 %). However, the influence of glucose on surface tension is fairly moderate (the surface tension of a 17 % mixture increases of less than 2 %, and the surface tension of a 55 %

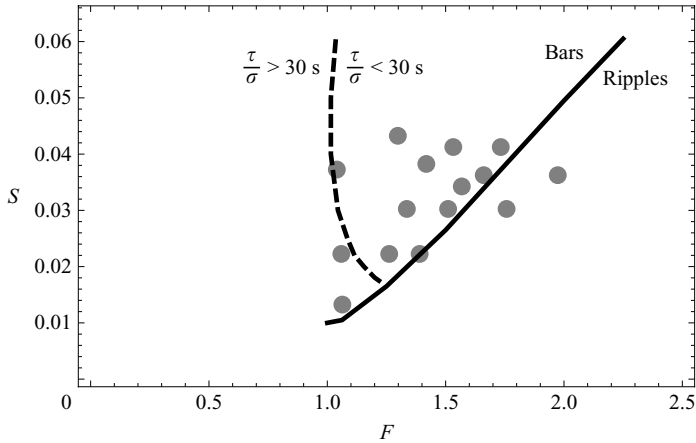


FIGURE 9. Existence diagram for the rhomboid pattern. Grey disks: experimental observation of a rhomboid pattern. These data correspond to a single viscosity ($\nu \approx 2.0 \times 10^{-6} \text{ m}^2 \text{ s}^{-1}$), so that the F and S are the only varying parameters. The solid line represents the theoretical transition from bars to ripples. The dashed line indicates a characteristic growth time equal to 30 s for the bar instability.

water–sucrose mixture increases of about 5 %, see Docoslis, Giese & van Oss 2000). In the following, we will thus consider that the surface tension of the mixture can be approached by the pure water value, that is, $74 \times 10^{-3} \text{ Nm}^{-1}$.

A run consisted in raking the sediment surface into a flat surface, before starting the flow. After a few seconds, a bed pattern forms, and its characteristics are recorded.

4.2. Experimental patterns and stability results

For each experimental run, the parameters Fr , Bo and Sh can be determined from the measured quantities (slope S , water discharge and viscosity), under the assumption of a Nußelt base state. The associated dispersion relation is then determined as described in §3. Figure 9 compares the theoretical existence domain for the rhomboidal pattern with the experiments. Only the experimental runs involving a single viscosity are represented on this figure, in order to reduce the parameter space to two dimensions. The experimental procedure was designed to focus on rhomboid patterns, and stable experiments were stopped, as well as those leading to ripple formation. The parameter space was intensely explored, and thus the absence of circle on diagram 9 indicates a domain where either ripples dominate the system, or no instability developed.

Rhomboidal patterns developed almost only where the linear stability analysis predicts their existence. Our stability analysis indicates that rhomboid patterns might also exist at low Froude numbers, but the observation time chosen during the experiment (between 30 and 60 s) kept Devauchelle *et al.* (2009) from recording them.

Nevertheless, rhomboidal patterns were never observed at high slope value (say above $S = 0.05$), even though they should exist according to the stability analysis. Neither the failure of the laminar assumption (which would involve a critical Reynolds number) nor the development of Kapitza wave (the system unstable with respect to these wave in the range of parameters where rhomboidal patterns were observed, see Yih 1963) can explain this observation. This point is still an open question.

In order to further test the predictions of the linear stability against experimental data, we have determined for every experimental run, the position and amplitude

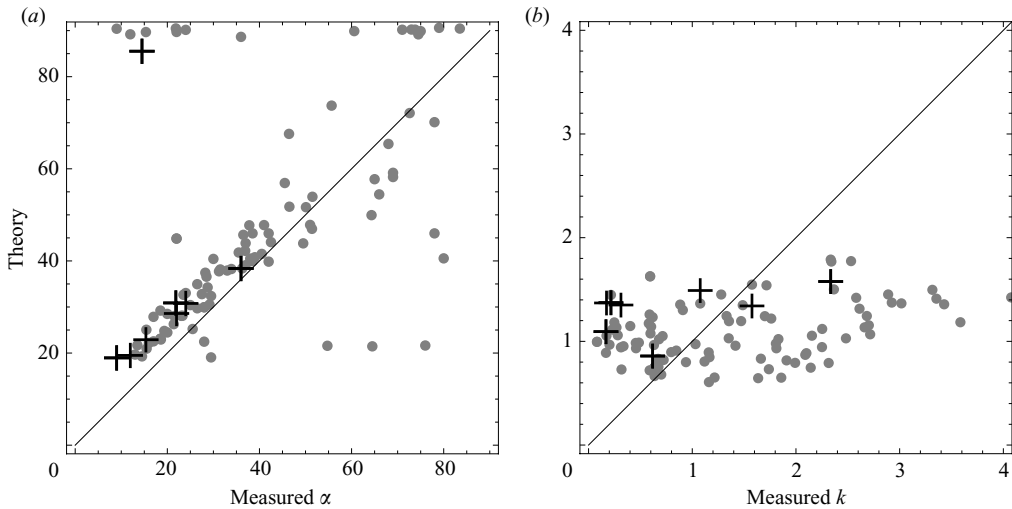


FIGURE 10. Comparison between the model presented in this paper, and the experimental results of Devauchelle *et al.* (2009). The comparison focuses on the geometrical characteristics of the rhomboid pattern: opening angle $\alpha = \pi/2 - \varphi$ (in degrees) and non-dimensional wavenumber k . The disks indicate a global maximum in the dispersion relation, whereas the crosses indicate only a local maximum. The sediment transport law employed here is a generalization in three dimensions of the model initially proposed by Charru & Hinch (2006). We used the flow parameters measured during the experiments for the stability analysis. The parameters of the erosion law are provided by Charru (2006). No additional free parameter was required for our analysis. On both plots, the solid line corresponds to the one-to-one relationship.

of the theoretical growth-rate maxima in the (k, ϕ) plane. Figure 10 compares these results to the geometrical characteristics of the experimental patterns.

The opening angle prediction is rather correct, given the measurement precision (about 10° , the pattern being usually fainter than it appears on figure 1). The large scatter (especially at high values of the angle α) is very likely due to inaccurate flow-parameters measurements. Indeed, as illustrated by figure 7, a small variation of a parameter in the neighbourhood of the ripple-bars transition can induce a large displacement of the most unstable mode.

The stability analysis is less accurate as regards the pattern wavelength. Indeed, even if the order of magnitude is correct, the theory predicts a rather constant wavenumber of order one, whereas the experimental data lie regularly between 0.1 and 4. We were not able to correct this tendency by tuning the empirical parameters of the sediment transport law.

5. Discussion and conclusion

The present paper proposes a natural framework to model the stability of laminar films with respect to sediment transport by bedload. It is shown that a generalization in three dimensions of the transport law proposed by Charru & Hinch (2006) and Charru (2006) can account for the beach rhomboid patterns initiation. It is thus fair to say that the diamond-shaped structures commonly observed on beaches are the laminar counterparts of alternate bars in rivers.

In return, since the rhomboid pattern is easily produced experimentally, it would be tempting to use it as a test case for sediment transport models. Their three-dimensional

structures add one more constraint on the bedload model (the opening angle) as compared to ripples. Transport laws are a key issue in geomorphology, and the bed slope influence on bedload remains a modelling challenge, especially in the transverse direction. Such an application of the present work would require that the flow model is correct. Such condition might not be fulfilled, especially at high values of the Reynolds number. Indeed, some of the discrepancy observed on figure 10 might be caused by the vorticity generated by the roughness of the sand surface, instead of some failure of the sediment transport law (as suggested by a referee of the present paper). In order to avoid this problem, one would have to limit the experiment to low Reynolds numbers, and to use a bed material as fine as possible.

The sediment transport law successfully used here was derived from a grains balance equation written for the bedload layer. This may indicate that laws for turbulent flows similarly derived could improve our understanding of rivers bedforms generation. This is the method used by Parker, Seminara & Solari (2003) to develop a new bedload transport model. To the heavy experiments conducted by Francalanci & Solari (2006) in order to evaluate the latter model, one could associate rhomboid pattern experiments, since these structures can also develop in turbulent flows (Morton 1978; Ikeda 1983). Interpreting such an experiment would require a three-dimensional stability analysis, with a turbulent flow and a free surface, similar to the one proposed by Besio, Blondeaux & Vittori (2006) for marine sand banks.

A next step towards the understanding of the rhomboid beach pattern would be to study its finite-amplitude behaviour, and particularly its saturation. Such an effort would allow to draw two new constraints on the sediment transport laws, namely the bedforms amplitude and velocity. As suggested by a reviewer of the present paper, the use of two-dimensional flow models of higher order than the Saint-Venant approximation (Scheid *et al.* 2006), instead of the full Navier–Stokes equations, would certainly facilitate such development. Numerical experiments in progress suggest that the nonlinearity in the sediment transport would be more important than the nonlinearity in the flow itself.

It is our pleasure to thank François Métivier, Clément Narteau, Stéphane Zaleski, Philippe Claudin and Bruno Andreotti for fruitful discussions. We also wish to express appreciation to Antonio Vieira and Yves Gamblin for the building of the experimental set-up. The first author was supported by a grant from the French Academy of Science.

REFERENCES

- ALLEN, J. R. L. 1982 *Sedimentary Structures – Their Character and Physical Basis, Vol. II*. Developments in Sedimentology, 30b, **663**, 395–405. Elsevier.
- ANDREOTTI, B., CLAUDIN, P. & DOUADY, S. 2002 Selection of dune shapes and velocities. Part 2. A two-dimensional modelling. *e Eur. Phys. J. B – Condens. Matter* **28** (3), 341–352.
- BAGNOLD, R. A. 1977 Bed load transport by natural rivers. *Water Resour. Res.* **13** (2), 303–312.
- BESIO, G., BLONDEAUX, P. & VITTORI, G. 2006 On the formation of sand waves and sand banks. *J. Fluid Mech.* **557**, 1–27.
- BLONDEAUX, P. & SEMINARA, G. 1985 A unified bar-bend theory of river meanders. *J. Fluid Mech.* **157**, 449–470.
- CALLANDER, R. A. 1969 Instability and river channels. *J. Fluid Mech.* **36**, 465–480.
- CHANG, H. Y. & SIMONS, D. B. 1970 The bed configuration of straight sand beds when flow is nearly critical. *J. Fluid Mech.* **42**, 491–495.
- CHARRU, F. 2006 Selection of the ripple length on a granular bed sheared by a liquid flow. *Phys. Fluids* **18**, 121508.

- CHARRU, F. & HINCH, E. J. 2006 Ripple formation on a particle bed sheared by a viscous liquid. Part 1. Steady flow. *J. Fluid Mech.* **550**, 111–121.
- CHARRU, F. & MOUILLERON-ARNOULD, H. 2002 Instability of a bed of particles sheared by a viscous flow. *J. Fluid Mech.* **452**, 303–323.
- CHARRU, F., MOUILLERON, H. & EIFF, O. 2004 Erosion and deposition of particles on a bed sheared by a viscous flow. *J. Fluid Mech.* **519**, 55–80.
- COLEMAN, S. E. & ELING, B. 2000 Sand wavelets in laminar open-channel flows. *J. Hydraul. Res.* **38** (5), 331–338.
- COLOMBINI, M. 2004 Revisiting the linear theory of sand dune formation. *J. Fluid Mech.* **502**, 1–16.
- COLOMBINI, M. & STOCCHINO, A. 2005 Coupling or decoupling bed and flow dynamics: fast and slow sediment waves at high Froude numbers. *Phys. Fluids* **17**, 036602.
- DEFINA, A. 2003 Numerical experiments on bar growth. *Water Resour. Res.* **39** (4), 1092.
- DEVAUCHELLE, O., JOSSEMAND, C., LAGRÉE, P. Y. & ZALESKI, S. 2007 Morphodynamic modelling of erodible laminar channels. *Phys. Rev. E* **76** (5), 56318.
- DEVAUCHELLE, O., MALVERTI, L., LAJEUNESSE, É., JOSSEMAND, C., LAGRÉE, P. Y. & MÉTIVIER, F. 2009 Rhomboid beach pattern: a pocket sized bedform. *J. Geophys. Res.* (submitted).
- DOCOSLIS, A., GIESE, R. F. & VAN OSS, C. J. 2000 Influence of the water–air interface on the apparent surface tension of aqueous solutions of hydrophilic solutes. *Colloids Surf. B: Biointerfaces* **19** (2), 147–162.
- ELBELRHITI, H., CLAUDIN, P. & ANDREOTTI, B. 2005 Field evidence for surface-wave-induced instability of sand dunes. *Nature* **437** (7059), 720–723.
- EXNER, F. M. 1925 Über die Wechselwirkung zwischen Wasser und Geschiebe in Flüssen. *Sitzberichte Akad. Wiss. Wien* **165** (3–4), 165–203.
- FRANCALANCI, S. & SOLARI, L. 2006 A particle tracking technique to study gravitational effects on bedload transport. In *River, Coastal, and Estuarine Morphodynamics: RCEM 2005: Proceedings of the 4th IAHR Symposium on River Coastal and Estuarine Morphodynamics, 4–7 October 2005*, Urbana, IL.
- HALL, P. 2006 Nonlinear evolution equations and the braiding of weakly transporting flows over gravel beds. *Stud. Appl. Math.* **117** (1), 27–69.
- HERSEN, P. 2004 On the crescentic shape of barchan dunes. *Eur. Phys. J. B – Condens. Matter Complex Syst.* **37** (4), 507–514.
- IKEDA, H. 1983 Experiments on bedload transport, bed forms, and sedimentary structures using fine gravel in the 4-meter-wide flume. *Environ. Res. Center Pap.* **2**, 1–78.
- IKEDA, S., PARKER, G. & SAWAI, K. 1981 Bend theory of river meanders. Part 1. Linear development. *J. Fluid Mech.* **112**, 363–377.
- KAPITZA, P. L. 1948 Wave motion of a thin layer of a viscous liquid I. *Zh. Eksp. Teor. Fiz* **18**, 3.
- KARCZ, I. & KERSEY, D. 1980 Experimental study of free-surface flow instability and bedforms in shallow flows. *Sedimentary Geol.* **27** (4), 263–300.
- KENNEDY, J. F. 1963 The mechanics of dunes and antidunes in alluvial channels. *J. Fluid Mech.* **16** (4), 521–544.
- KNAAPEN, M. A. F. & HULSCHER, S. 2003 Use of a genetic algorithm to improve predictions of alternate bar dynamics. *Water Resour. Res.* **39** (9), 1231.
- KOUAKOU, K. K. J. & LAGRÉE, P. Y. 2005 Stability of an erodible bed in various shear flows. *Eur. Phys. J. B – Condens. Matter* **47** (1), 115–125.
- KURU, W. C., LEIGHTON, D. T. & MCCREADY, M. J. 1995 Formation of waves on a horizontal erodible bed of particles. *Intl J. Multiph. Flow* **21** (6), 1123–1140.
- LAGRÉE, P. Y. 2000 Erosion and sedimentation of a bump in fluvial flow. *Comptes Rendus de l'Académie des Sciences Séries IIB Mechanics* **328** (12), 869–874.
- LAGRÉE, P. Y. 2003 A triple deck model of ripple formation and evolution. *Phys. Fluids* **15**, 2355.
- LAJEUNESSE, E., MALVERTI, L., LANCIEN, P., ARMSTRONG, L., MÉTIVIER, F., COLEMAN, S., SMITH, C., DAVIES, T., CANTELLI, A. & PARKER, G. 2009 Fluvial and subaqueous morphodynamics of laminar and near-laminar flows: a synthesis. *Sedimentology* (in press).
- LANGLOIS, V. & VALANCE, A. 2005 Formation of two-dimensional sand ripples under laminar shear flow. *Phys. Rev. Lett.* **94** (24), 248001.

- LIN, S. P. & CHEN, J. N. 1997 Elimination of three-dimensional waves in a film flow. *Phys. Fluids* **9**, 3926.
- MORTON, R. A. 1978 Large-scale rhomboid bed forms and sedimentary structures associated with hurricane washover. *Sedimentology* **25**, 183–204.
- PARKER, G., SEMINARA, G. & SOLARI, L. 2003 Bed load at low Shields stress on arbitrarily sloping beds: alternative entrainment formulation. *Water Resour. Res.* **39** (7), 1183.
- REYNOLDS, A. J. 1965 Waves on the erodible bed of an open channel. *J. Fluid Mech.* **22**, 113–133.
- SAUERMAN, G., KROY, K. & HERRMANN, H. J. 2001 Continuum saltation model for sand dunes. *Phys. Rev. E* **64** (3), 31305.
- SCHEID, B., RUYER-QUIL, C. & MANNEVILLE, P. 2006 Wave patterns in film flows: modelling and three-dimensional waves. *J. Fluid Mech.* **562**, 183–222.
- SHIELDS, A. 1936 *Anwendung der Aehnlichkeitsmechanik und der Turbulenzforschung auf die Geschiebebewegung*. Preussische Versuchsanstalt für Wasserbau und Schiffbau.
- SINGH, I. B. 1969 Primary sedimentary structures in Precambrian quartzites of Telemark, Southern Norway and their environmental significance. *Nor. Geol. Tidsskr.* **49**, 1–31.
- STAUFFER, M. R., HAJNAL, Z. & GENDZWILL, D. J. 1976 Rhomboidal lattice structure: a common feature on sandy beaches. *Can. J. Earth Sci.* **13** (12), 1667–1677.
- THOMPSON, W. O. 1949 Lyons sandstone of Colorado Front Range. *AAPG Bull.* **33** (1), 52–72.
- VALANCE, A. & RIOUAL, F. 1999 A nonlinear model for aeolian sand ripples. *Eur. Phys. J. B – Condens. Matter* **10** (3), 543–548.
- WILLIAMSON, W. C. 1887 On some undescribed tracks of invertebrate animals from the Yoredale rocks, and on some inorganic phenomena, produced on tidal shores, simulating plant remains. *Manchester Lit. Phil. Soc. Mem. Proc., Ser. 3* (10), 19–29.
- WOODFORD, A. O. 1935 Rhomboid ripple mark. *Am. J. Sci., 5th Ser.* **29**, 518–525.
- YIH, C. S. 1963 Stability of liquid flow down an inclined plane. *Phys. Fluids* **6**, 321–334.